

RESEARCH ARTICLE | NOVEMBER 01 2023

Pulsed laser ablation synthesis of Cu-based and Ni-based nanostructured electrodes for highly active alkaline oxygen and hydrogen evolution reactions

V. Iacono ; C. Lo Pò ; S. Scalese ; S. Boninelli; G. G. Condorelli ; M. G. Grimaldi ; F. Ruffino 



APL Mater. 11, 111102 (2023)

<https://doi.org/10.1063/5.0169678>



CrossMark


AMERICAN ELEMENTS
THE ADVANCED MATERIALS MANUFACTURER®

yttrium iron garnet, zeolites, nano ribbons, sapphire windows, spintronics, silver nanoparticles, MOCVD, rare earth metals, osmium, refractory metals, anodic titanium niobate, perovskite crystals

glassy carbon, III-IV semiconductors, barium fluoride, epitaxial crystal growth, cerium oxide polishing powder, surface functionalized nanoparticles, beta-barium borate, quantum dots, scintillation Ce:YAG, laser crystals, niobate, InAs wafers, MOFs, AuNPs, ZnS, CdTe, transparent ceramics

beamsplitters, gallium lump, europium phosphors, ultra high purity materials, transparent ceramics, CIGS, cermet, nanodispersions, MBE grade materials, thin film, OLED lighting, solar energy, sputtering targets, fiber optics, h-BN, deposition slugs, CVD precursors, photovoltaics, metamaterials, borosilicate glass, YBCO superconductors, InGaAs, indium tin oxide, MgF2, rutile, diamond micropowder, optical glass

additive manufacturing, organometallics, infrared dyes, transparent ceramics, CIGS, cermet, nanodispersions, MBE grade materials, thin film, OLED lighting, solar energy, sputtering targets, fiber optics, h-BN, deposition slugs, CVD precursors, photovoltaics, metamaterials, borosilicate glass, YBCO superconductors, InGaAs, indium tin oxide, MgF2, rutile, diamond micropowder, optical glass



Now Invent.™

www.americanelements.com

© 2001-2022, American Elements LLC, a U.S. Registered Trademark

Pulsed laser ablation synthesis of Cu-based and Ni-based nanostructured electrodes for highly active alkaline oxygen and hydrogen evolution reactions

Cite as: APL Mater. 11, 111102 (2023); doi: 10.1063/5.0169678

Submitted: 27 July 2023 • Accepted: 12 October 2023 •

Published Online: 1 November 2023









View Online



Export Citation



CrossMark

V. Iacono,^{1,2,a)}  C. Lo Pò,^{1,b)}  S. Scalese,³  S. Boninelli,³  G. G. Condorelli,^{4,5}  M. G. Grimaldi,^{1,2}  and F. Ruffino^{1,2,5} 

AFFILIATIONS

¹ Dipartimento di Fisica e Astronomia "Ettore Majorana," Università di Catania, Via S. Sofia 64, 95123 Catania, Italy

² CNR-IMM, Via S. Sofia 64, 95123 Catania, Italy

³ CNR-IMM, Strada VIII n.5, 95121 Catania, Italy

⁴ Department of Chemical Sciences, University of Catania, Viale Andrea Doria 6, 95123 Catania, Italy

⁵ Research Unit of the University of Catania, National Interuniversity Consortium of Materials Science and Technology (INSTM-UdR of Catania), Viale Andrea Doria 8 and Via S. Sofia 64, 95125 Catania, Italy

^{a)} Author to whom correspondence should be addressed: valentina.iacono@dfa.unict.it

^{b)} cristiano.lopo@dfa.unict.it

ABSTRACT

In the field of sustainability, hydrogen (H₂) is considered a clean fuel and a renewable energy source with no pollutant emissions. The production of H₂ by water electrolysis is well-known among the scientific community. Still, alkaline electrolysis represents a challenging process and requires expensive materials have to be avoided in order to lower the impact of H₂ production. This work deals with the production of copper (Cu) and nickel (Ni) nanoparticles (NPs) as catalysts for alkaline water splitting reactions. These NPs are synthesized using the pulsed laser ablation in liquid involving the ablation of Cu and Ni targets in methanol and ethanol. The morphological, structural, and compositional properties of the obtained NPs are studied. Then, a low amount of NPs-based catalyst ($\sim 1 \mu\text{g}/\text{cm}^2$) was loaded onto a nickel foam substrate and tested for both alkaline Hydrogen Evolution Reaction (HER) and Oxygen Evolution Reaction (OER). The best performance at 10 mA cm^{-2} , in terms of overpotential (η), for OER was shown by Ni NPs, $\eta = 327 \text{ mV}$, while for the HER, Cu NPs reached $\eta = 211 \text{ mV}$ at 10 mA cm^{-2} in aqueous 1M KOH. The ultra-low amount of the catalyst material makes these electrodes challenging in terms of mass activity [up to 14 A/mg at 10 mA cm^{-2}] compared to the state of the art. In addition, the correlation between overpotential and the availability of electrons at the surface of the catalyst for H₂ production was studied by using Mott-Schottky analysis.

© 2023 Author(s). All article content, except where otherwise noted, is licensed under a Creative Commons Attribution (CC BY) license (<http://creativecommons.org/licenses/by/4.0/>). <https://doi.org/10.1063/5.0169678>

I. INTRODUCTION

Hydrogen, as an energy vector, represents the new frontier of sustainability due to its abundance, different ways of production, and high energy conversion efficiencies.¹ The most simple and efficient way to produce hydrogen is the electrolysis of water, exploiting the reaction $2\text{H}_2\text{O} \rightarrow 2\text{H}_2 + \text{O}_2$. In an electrolyzer, a voltage is applied between a cathode and an anode immersed into

an electrolyte. Specifically, at the cathode, hydrogen is produced through Hydrogen Evolution Reaction (HER), while at the anode, the Oxygen Evolution Reaction (OER) occurs. At present, an alkaline environment is becoming preferred for an electrolyzer in order to avoid corrosion related issues. However, a good HER performance in an alkaline electrolyte is still challenging to achieve.² The best performing material for alkaline HER is reported to be platinum, while the best performing material for OER³ is RuO₂. These

materials are precious, rare, and difficult to mine, so a sustainable and affordable alternative is required.² A variety of nanomaterials have been reported in the literature, which could be chosen as catalysts in renewable energy systems. Transition metal oxides and their perovskites have attracted much interest, and their applications on energy systems are still largely investigated.^{4,5} Transition metals (Cu, Ni, Fe, etc.) and their oxides have attracted much interest due to their abundance and lower cost, have widely been reported for electrocatalyst production, and represent eco-friendly alternatives to rare or toxic elements or compounds. These transition metals occupy a high position in the volcano plot for HER,⁶ not far from platinum, indicating a good catalytic activity. Beyond the choice of catalyst materials, the amount of catalysts and their nanostructure should also be considered in evaluating the intrinsic catalytic activity.^{2,3,7–10}

Pulsed Laser Ablation in Liquid (PLAL) represents a valid synthesis route for the production of nanoparticles (NPs). This technique is cost-effective and does not require high temperature or high pressure facilities.¹¹ It represents an alternative to chemical-based approaches because of the decreased by-product waste and no need for further surfactants. PLAL involves a high energy pulsed laser that is focused on a target immersed in a liquid. The high power focused in a small area leads to the creation of a plasma containing the ablated target material. A cavitation bubble is formed involving reactions with the surrounding liquid, and finally, NPs are released in the liquid. By tuning the different laser parameters (fluence, wavelength, pulse duration, repetition rate, etc.), it is possible to change the morphological and structural NP characteristics.¹² In particular, the fluence parameter (defined as pulse energy over laser spot area [J/cm^2]) controls the NP size.¹³ This technique is reported to bring the formation of pure or defected nanocrystals.¹⁴ The literature reports that using water as a liquid, transition metal oxide NPs can be obtained. The organic solvents (methanol, ethanol, etc.), instead, typically lead to metallic NPs.^{15–17} In this work, copper (Cu) and nickel (Ni) NPs are synthesized with PLAL in methanol and ethanol. These NPs are loaded on a Nickel Foam (NF) substrate in order to fabricate the electrodes tested for both alkaline HER and OER.

II. MATERIALS AND METHODS

A. NP synthesis

Copper and nickel NPs are synthesized using a Nd:YAG ns-pulsed laser (Quanta-Ray Pro Series Nd:YAG laser with wavelength $\lambda = 1064$ nm, pulse length = 12 ns, mean power = 5 W, and repetition rate = 10 Hz). The high-power laser beam was focused through a lens (a focal length of 10 cm) on the metal (Cu and Ni) target placed at the bottom of a Teflon vessel, filled with 8 ml of liquid (methanol and ethanol) (1a). Three NP dispersions were produced: Cu NPs in methanol (Cu_{met}), copper NPs in ethanol (Cu_{et}), and Ni NPs in methanol (Ni_{met}). The targets were weighed with a Sartorius ME5 microbalance (sensitivity: 0.01 mg) before and after each ablation to evaluate the ablated mass. The NP dispersions obtained were stored at 4 °C in order to prevent agglomeration.

B. NP characterization

The NP dispersions were optically analyzed using a Varian Cary 500 UV-Vis-NIR Spectrophotometer measuring the

absorbance from 200 to 1080 nm. The morphological characterization and structural characterization were performed using a Gemini field emission SEM Carl Zeiss SUPRA 25 scanning electron microscope [FEG-SEM], Zeiss SUPRA 35 FE-SEM, and JEOL 2010F Transmission Electron Microscope (TEM) at a primary beam energy of 200 keV. The NPs were prepared for TEM analysis by drop casting the NPs dispersion onto a Lacey carbon supported gold TEM grid. The TEM images were analyzed using the DigitalMicrograph software. The size distribution for each NP dispersion was obtained from the TEM images. The crystalline phase of NPs was determined by the X-Ray Diffraction (XRD) analysis in the grazing incidence mode ($\theta_{inc} = 0.2^\circ$) using a SmartLab Rigaku diffractometer, equipped with a rotating anode of Cu (radiation = 1.541 84 Å) operating at 45 kV and 200 mA. For the XRD measurements, the NPs dispersion was drop cast on a Corning Glass substrate. The NPs surface was analyzed with the X-Ray Photoelectron Spectroscopy (XPS) at a 45X takeoff angle relative to the surface sample holder, with a PHI 5000 VersaProbe II system (ULVAC-PHI, Inc.; the base pressure of the main chamber is $1 \cdot 10^{-8}$ Pa). The samples were excited with the monochromatized Al $K\alpha$ x-ray radiation using a pass energy of 5.85 eV.

C. Electrode preparation

Each electrode was obtained by drop casting 60 μl of NP dispersion on 1 cm^2 of a Nickel Foam (NF) substrate (Goodfellow Inc., Huntingdon, England; thickness 1.6 mm and porosity $\geq 95\%$). This substrate was rinsed before with deionized water and dried with N_2 . After the NP loading, the electrodes were placed on a hot plate ($\sim 80^\circ\text{C}$) to have the complete evaporation of the solvent. The electrode production scheme is presented in Fig. S1. For each electrode, the amount of the catalyst loading, m , was estimated by Rutherford Backscattering Spectrometry (RBS) using 2 MeV He^+ ions at normal incidence with 165° detector angle. In order to perform RBS measurements, 60 μl of NPs dispersion was drop cast onto a graphene paper substrate. The catalyst loading was evaluated by integrating the related element peak with the XRump software.¹⁸ The catalyst loading follows from the measured atomic density by¹⁹

$$\text{Catalyst loading}[\text{mg}/\text{cm}^2] = \frac{\text{Dose}[\text{at}/\text{cm}^2]}{N_A[\text{at}/\text{mol}]} M[\text{g}/\text{mol}], \quad (1)$$

where N_A is the Avogadro number and M is the molar mass.

D. Electrochemical characterization

The electrochemical measurements have been performed under alkaline conditions (aqueous 1M KOH, pH = 14). A three-electrode setup (using a VersaSTAT 4 potentiostat) with a platinum wire as the cathode and a saturated calomel electrode (SCE) as the reference electrode has been used. After cyclic voltammetry (CV) for the electrode stabilization, the HER and OER activities were investigated using linear sweep voltammetry (LSV), Electrochemical Impedance Spectroscopy (EIS), and the Mott-Schottky (MS) analysis.

The CV and LSV were performed, respectively, at 10 and 5 mV/s in the range -1.5 to 0 V for HER and 0 to 0.7 V for OER

with respect to SCE. The obtained potentials vs RHE were corrected by iR_u compensation,

$$\eta = E_{RHE} - iR_u, \quad (2)$$

where i is the measured current and $R_u[\Omega]$ is the uncompensated resistance. This resistance was obtained with EIS executed in the range 0.1 Hz–100 kHz at the onset potential. The EIS data were fitted with an Armstrong and Henderson^{20–22} equivalent circuit using the EIS spectrum analyzer software.²³

The mass activity is evaluated at the given current density of $j = 10 \text{ mA/cm}^2$ from the catalyst loading as

$$\text{Mass activity [A/mg]} = \frac{j[\text{A/cm}^2]}{\text{Catalyst loading [mg/cm}^2]}. \quad (3)$$

The chronopotentiometry (CP) measurements were conducted in an aqueous 1M KOH solution for 13h at a constant current density of 10 mA cm^{-2} . For this long-term stability measurement, the CP was performed using mercury/mercury oxide (Hg/HgO, saturated in 1M NaOH) as the reference electrode to avoid the instability effect of the SCE.

The MS analysis was conducted in the range -1.0 to 1.0 V vs SCE at 1 kHz. The flat band potential V_{fb} is extracted from the

x-intercept by the linear fit of the linear region in the Mott–Schottky plot.^{24,25} The Mott–Schottky equation is given by

$$\frac{1}{C^2} = \frac{2}{\epsilon\epsilon_0 A^2 e N_D} \left(V - V_{fb} - \frac{k_B T}{e} \right), \quad (4)$$

where C is the measured capacitance at the given voltage V , ϵ and ϵ_0 are the dielectric constants, A is the electrode surface, e is the electron charge, N_D is the number of donors, and $\frac{k_B T}{e}$ is the thermal correction with k_B being the Boltzmann constant and $T = 25^\circ \text{C}$. From the flat band potential, the band bending V_{bb} is given by¹⁹

$$V_{bb} = V_{fb} - V_{oc}, \quad (5)$$

where V_{oc} is the open circuit (OC) potential: the potential of the electrode with respect to SCE without any applied potential at equilibrium.

III. RESULTS AND DISCUSSIONS

A. Morphological and structural characterization and consideration

Figure 1(a) shows the scheme of the PLAL synthesis. The laser beam is focused onto a vessel containing the liquid environment in which the metallic target is immersed. After 10 min of ablation, the NPs are released into the liquid. The PLAL NP dispersion synthesis details and the parameters are reported in Table I.

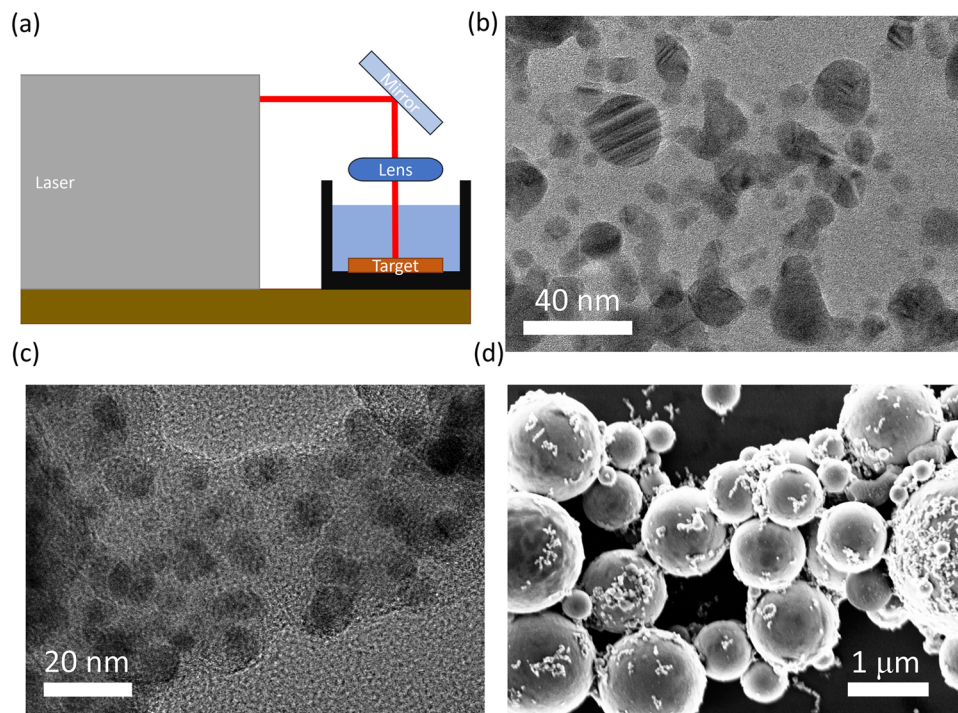


FIG. 1. (a) PLAL scheme setup. (b) TEM image of the Cu_{met} obtained dispersion. (c) TEM image of the Cu_{et} obtained dispersion. (d) SEM image of the Ni_{met} obtained dispersion drop cast on the silicon substrate.

TABLE I. NP synthesis parameters: target, solvent, ablation time, and ablated mass with an error of 0.02 mg.

Dispersion	Target	Solvent	Ablation time (min)	Ablated mass (mg)
<i>Cu_met</i>	Copper	Methanol	10	0.09
<i>Cu_et</i>	Copper	Ethanol	10	0.13
<i>Ni_met</i>	Nickel	Methanol	10	0.40

TABLE II. Log-normal distribution parameters for particles radius extracted by the SEM and TEM images. x_c is the distribution median, w is the scale parameter, and n indicates the particle number used for the statistic.

Sample	SEM distribution			TEM distribution		
	x_c (nm)	w	n	x_c (nm)	w	n
<i>Cu_met</i>	47	0.67	1008	2.1	0.62	892
<i>Cu_et</i>	43	0.69	135	3.3	0.52	130
<i>Ni_met</i>	484	0.47	487

After the NP synthesis, the UV-Vis absorption measurements were performed. The absorbance spectra (Fig. S2 of the supplementary material) revealed the plasmonic peaks of copper for both the *Cu_Met* and *Cu_Et* dispersions and the plasmonic peak of nickel for *Ni_Met*.²⁶

The SEM images show spherical particles for the three samples (see the supplementary material). The TEM images [Figs. 1(b) and 1(c)] acquired for Cu-based NP dispersion allowed to resolve the smaller particles (of some nanometers) not sufficiently resolved with the SEM analysis. Some of the large NPs observed with the TEM appeared to form agglomerates of small particles; thus, they were not taken into account for the size distribution. The presence of a layer embedding the NPs and with different chemical compositions with respect to the NPs is evident in the *Cu_et* sample [Fig. 1(c)]. No evidence of shell around the NPs was found. Figure 1(d) shows a SEM image of Ni NPs. For this sample, due to the predominance of bigger NPs, TEM measurements were not performed. As also shown

in Fig. S4(a), Ni NPs tend to form linear chains, possibly due to the magnetic features of the material.

The NP size distributions obtained by analyzing TEM and SEM images [Figs. 1(b) and 1(c)] show a log-normal trend, as already reported in the literature regarding the PLAL-based NP production.¹¹ The log-normal distribution equation is given by

$$f(x) = \frac{1}{xw\sqrt{2\pi}} \exp\left(-\frac{\ln^2(x/x_c)}{2w^2}\right), \quad (6)$$

where x_c is the median of the distribution and w is the scale parameter related to the distribution width.^{27,28} Table II presents the outcomes of the size distribution derivation with the relative parameters referred to in Eq. (6).

The high-resolution (HR)-TEM revealed that the crystalline phase and single atomic planes of NPs can be distinguished [Fig. 2(a)]. The interplanar distance was measured for some different *Cu_met* NPs with a direct line profile method measurement using the Digital Micrograph software.²⁹ The mean values of interplanar distances were measured in different regions of the particle, as shown in Fig. 2(a). The mean value found was 2.2 with a standard deviation of 0.2 Å. Cu(1, 1, 1) and its oxide CuO(1, 1, 1) interplanar distances are, respectively, 2.087 Å and 2.316 Å (obtained using the CaRIne Crystallography software³⁰). The HR-TEM derived information on the interplanar distance is not sufficient in order to distinguish if the NPs are Cu or CuO. Thus, a direct diffraction measurement was performed. The right half of Fig. 2(c) shows the acquired diffraction pattern of *Cu_met* NPs. The left half of Fig. 2(c), instead, shows the metallic Cu rings simulated with the CrystBox software.³¹ The match between the simulated and experimental patterns confirms the metallic structure of the NPs obtained by ablating copper in methanol. In Fig. S6, the acquired diffraction pattern for the *Cu_met* NPs is compared with the theoretical values of CuO and Cu₂O, highlighting that the data agree with the Cu, as shown in Fig. 2(c).

The same analysis for *Cu_et* NPs was hard to achieve due to the embedding thick layer: the atomic planes were recognizable and measurable only for few NPs. The mean values of interplanar distance are 2.1 ± 0.1 Å by the line profile method and 2.1 ± 0.2 Å by the Fast Fourier Transform (FFT) method, which agrees with the metallic Cu phase.

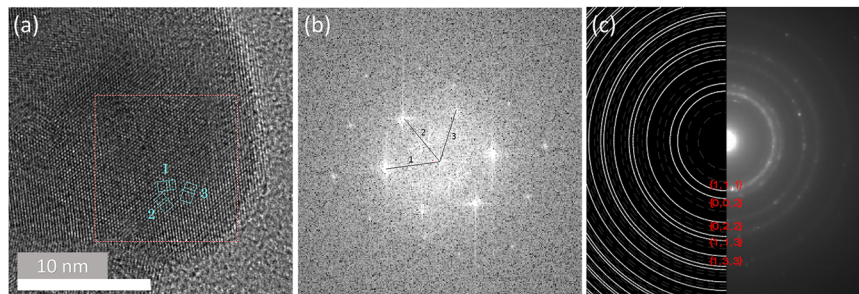


FIG. 2. (a) *Cu_met* particle with clearly visible atomic planes in three crystallographic directions (marked with numbers). (b) FFT of the red dashed square in (a), with the corresponding crystallographic directions; six spots are clearly visible, but the second order spots are also visible. (c) Measured direct diffraction of *Cu_met* compared to simulated rings of metallic Cu obtained with Ref. 31, along with the corresponding Miller indices.

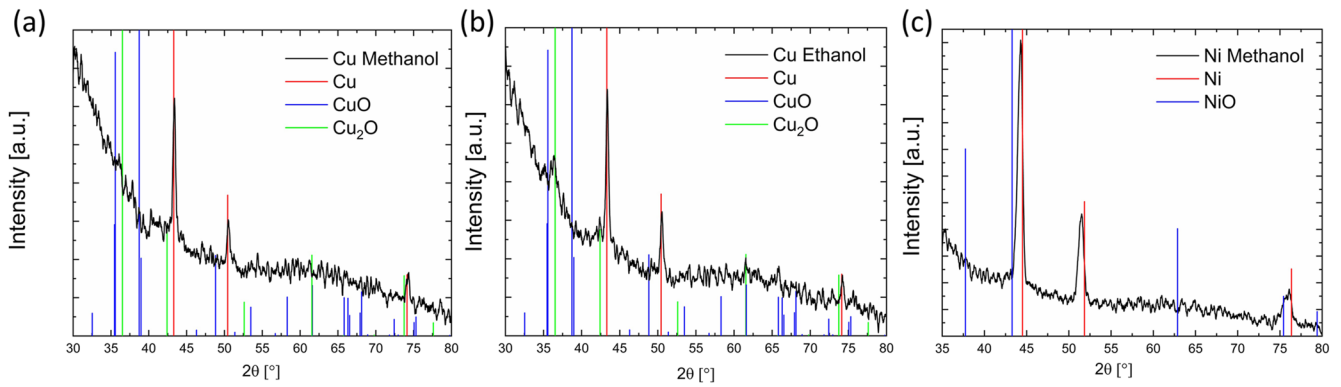


FIG. 3. XRD patterns of (a) *Cu_met*, (b) *Cu_et*, and (c) *Ni_met* NPs deposited on the Corning Glass substrate. The vertical lines indicate the position and intensity of XRD peaks referring to Cu,³² CuO,³³ Cu₂O,³⁴ Ni,³⁵ and NiO.³⁶

The XRD measurements were performed at 0.2° grazing angle in the range $2\theta = 35^\circ - 80^\circ$ in order to get more details on the structural properties of the produced NPs. The XRD patterns (linear scale) of the three samples are shown in Fig. 3. In all the three patterns, the metallic nature of the NPs is highlighted. The copper

NPs produced in both methanol and ethanol show peaks at $\sim 43^\circ$, $\sim 50^\circ$, and $\sim 70^\circ$, indicating, respectively, Cu(1, 1, 1), Cu(2, 0, 0), and Cu(2, 2, 0) planes³² with no evident presence of oxides.^{33,34} Only in the *Cu_et* sample, a partial oxidation is indicated by the Cu₂O related peak at $\sim 36^\circ$. The nickel NP pattern shows peaks at $\sim 44^\circ$,

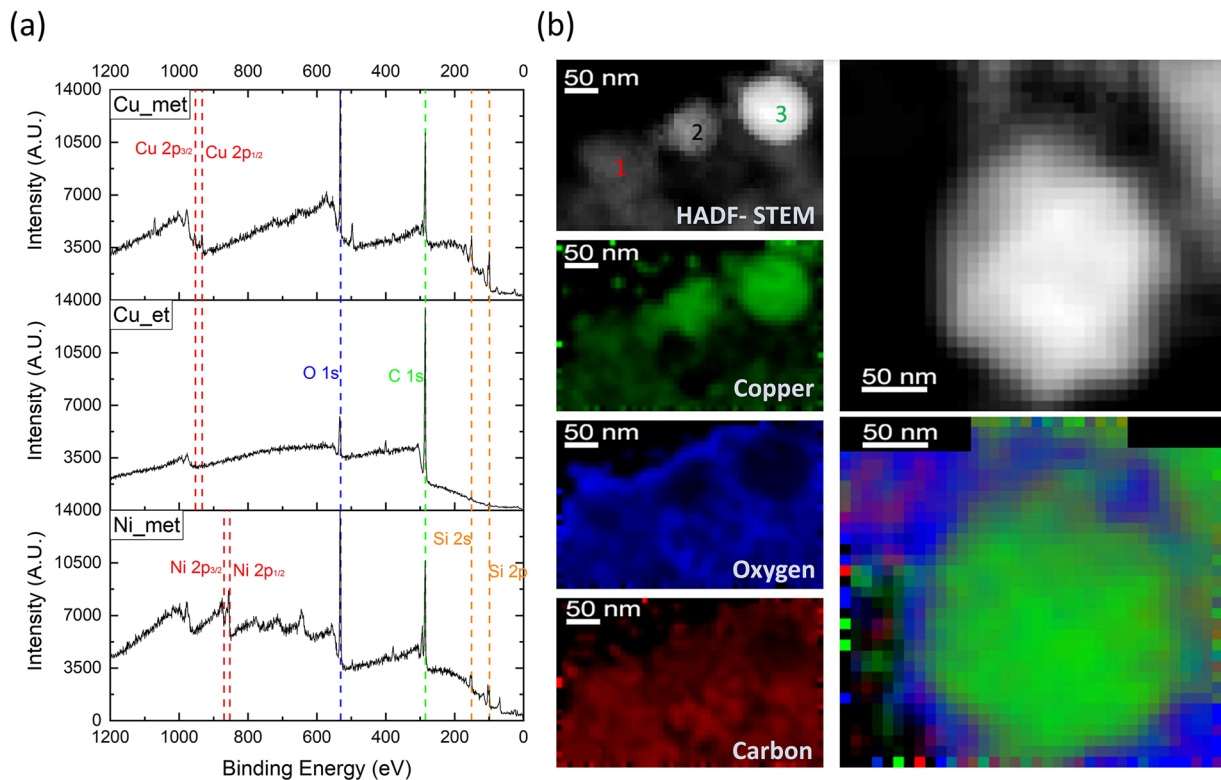


FIG. 4. (a) XPS spectrum of (from top to bottom) *Cu_met*, *Cu_et*, and *Ni_met* NPs on silicon with vertical dashed lines indicating literature peaks³⁸ for Cu, Ni, O, C, and Si. (b) Collection of STEM-EDX images representing different elemental compositions with color maps (green → copper, blue → carbon, and red → oxygen). Then, the overlap of the color map with the acquired HADF-STEM image of the particle.

28 November 2023 07:41:58

TABLE III. RBS measured dose and evaluated catalyst loading for each electrode.

Electrode	Dose (at cm ⁻²)	Catalyst loading (μg cm ⁻²)
<i>Cu_met</i>	7.73×10^{15}	0.8
<i>Cu_et</i>	1.08×10^{16}	1.1
<i>Ni_met</i>	7.35×10^{15}	0.7

~51°, and ~76°, indicating, respectively, Ni(1, 1, 1), Ni(2, 0, 0), and Ni(2, 2, 0) planes.³⁵ Still, no trace of oxides³⁶ is present, but all the peaks are shifted at lower angles, maybe due to a starting carbonization occurring in the outer surface of NPs.³⁷

1. NP composition

Figure S10 of the supplementary material shows the high-resolution XPS spectra showing each element region. The XPS

survey spectra [Fig. 4(a)] indicate, for all the particles, a strong presence of carbon (peak at ~285 eV) and oxygen (peak at ~531 eV and Auger peak at ~978 eV) on the surface. In addition, the silicon substrate (peaks at³⁸ ~151 eV and ~99 eV) is visible in the *Cu_met* and *Ni_met* samples. The oxygen presents a chemical shift (532.6, 533.6, and 532.6 eV, respectively, in *Cu_met*, *Cu_et*, and *Ni_met*), which suggests the presence of SiO₂.³⁸ The carbon signal also presents a shift (285.7, 285.6, and 286 eV, respectively, in *Cu_met*, *Cu_et*, and *Ni_met*), which can be attributed to the presence of alcohols.³⁸ The copper peak at ~933 eV in *Cu_met* suggests an intermediate nature of metallic *Cu* and *CuO*. However, the absence of the oxide satellite peak can support the metallic composition.³⁸ The peaks of copper in *Cu_et* are absent, and the silicon ones are really low in intensity. This can suggest that the layer embedding the NPs in this case and as seen in TEM images (Fig. 1) is actually screening the copper signal. This matrix is made up of carbon and oxygen and is shown in Fig. 2; its thickness should be in the order of tens of nanometers. This thick

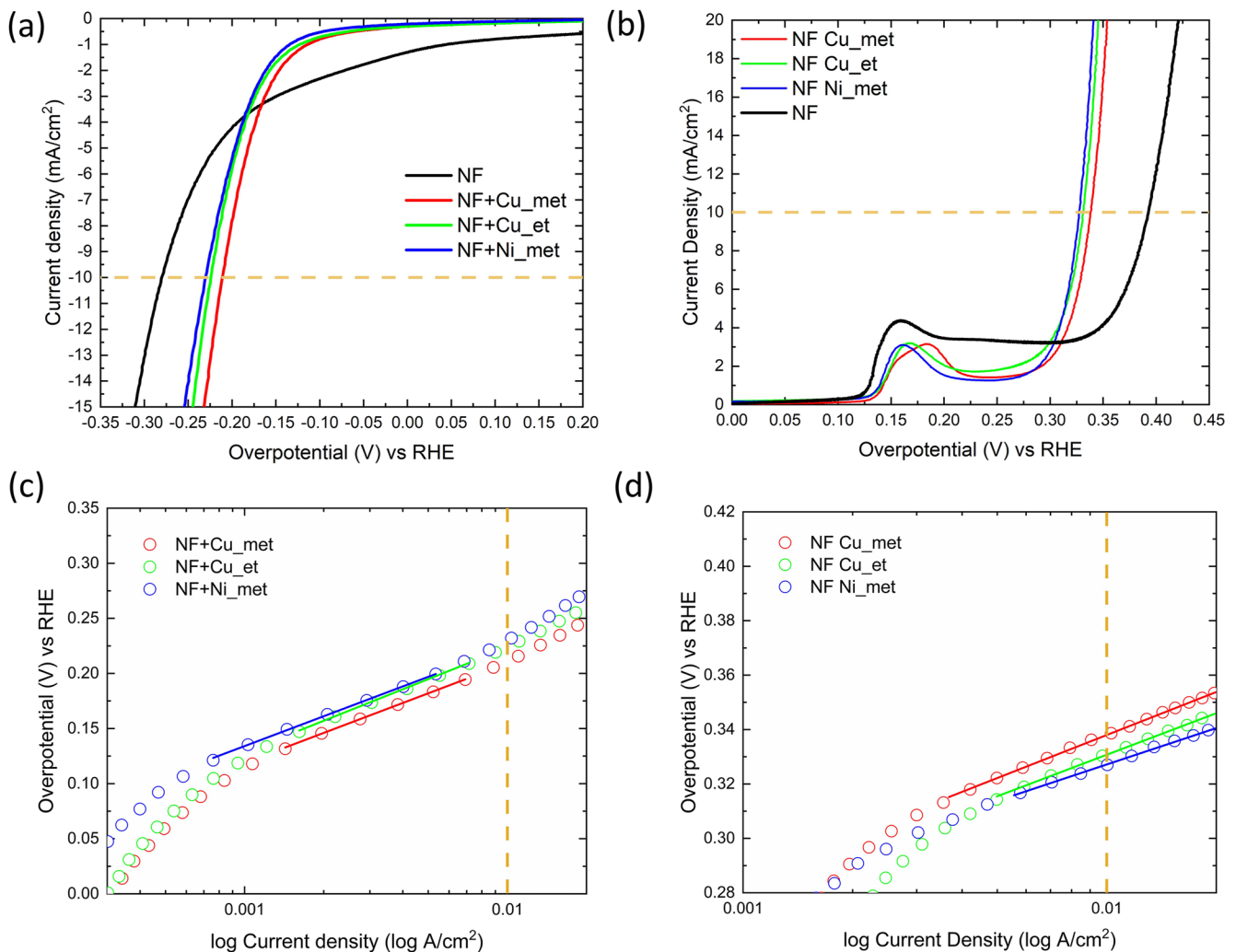


FIG. 5. (a) LSV curves for HER and (b) LSV curves for OER of NPs loaded onto NF. (c) Tafel plot of HER and (d) Tafel plot of OER. The horizontal orange dashed lines in (a) and (b) and the vertical orange dashed lines in (c) and (d) mark the current density of 10 mA/cm².

layer should be able to hide the presence of copper from the XPS source. The nickel sample presents its peak at ~ 856 eV, suggesting some carbon compounds at least on the surface of NPs.³⁸

The Scanning Transmission Electron Microscope - Energy Dispersive X-Ray (STEM-EDX) image [Fig. 4(b)] shows a color map of *Cu_met* NPs, indicating how copper, carbon, and oxygen are distributed: the NPs are purely metallic, while carbon and oxygen are uniformly distributed outside the NPs. The particle marked as “3” appears brighter than the others and, in fact, presents a higher copper intensity. The other particles marked as “2” and “1” are embedded (“1” more than “2”), and, hence, they appear less brilliant, and the copper intensity is much lower for both, while the carbon and oxygen intensities are higher. The image collecting all the elements’ signal indicates that both carbon and oxygen take place outside the Cu particle.

In the literature, it is well known that the presence of both alcohol vapor and plasma leads to the formation of some polymers, as shown using a UV laser,^{39,40} using an RF electric field between two electrodes,^{41,42} or with PLAL using a graphite target.⁴³ The substance found in this work is made up of carbon and oxygen, and it may even be an organic layer, perhaps a polymeric layer. Another possible explanation for the presence of carbon and oxygen regards the adsorption of alcohol molecules on the surface of the metal and, eventually, their dissociation, as was observed in TiO₂ NPs in ethanol.⁴⁴ Indeed, further studies and chemical characterization should be conducted to confirm this hypothesis.

B. Electrochemical characterization

Electrodes for electrochemical characterization were prepared as described in Sec. II C. In the supplementary material, the RBS spectra from which the catalyst loading was extracted are reported. The integral of the peak referred to Ni or Cu resulted in the dose value in at/cm^2 . The dose and the catalyst loading values are reported in Table III.

The electrochemical measurements were performed in aqueous 1M KOH. The *iR* corrected LSV measurements are plotted in Fig. 5(a) (HER) and Fig. 5(b) (OER). Compared to the bare substrate, the NPs showed an improved catalytic activity. Indeed, the best HER electrode was found to be the *Cu_met* NPs loaded NF, which showed an overpotential at 10 mA cm^{-2} of 211 mV vs RHE. The best OER activity was shown by the *Ni_met*-loaded NPs with an overpotential of 327 mV vs RHE.

The Tafel plots are shown in Figs. 5(c) and 5(d). The Tafel slope for the HER electrodes shows the values of $\sim 90 \text{ mV dec}^{-1}$. The best electrode for OER, the *Ni_met*, showed a Tafel slope of 44 mV dec^{-1} , which agrees with the Volmer-step as a rate determining step.

The stability of the electrode showing the lowest overpotential for the HER was tested over 13 h with a chronopotentiometry measurement [Fig. 6(a)]. After this measurement, the overpotential increased by 10% at $10 \text{ mA}/\text{cm}^2$.

In order to investigate the band energy bending role in the catalytic activity, the Mott-Schottky analysis was performed.

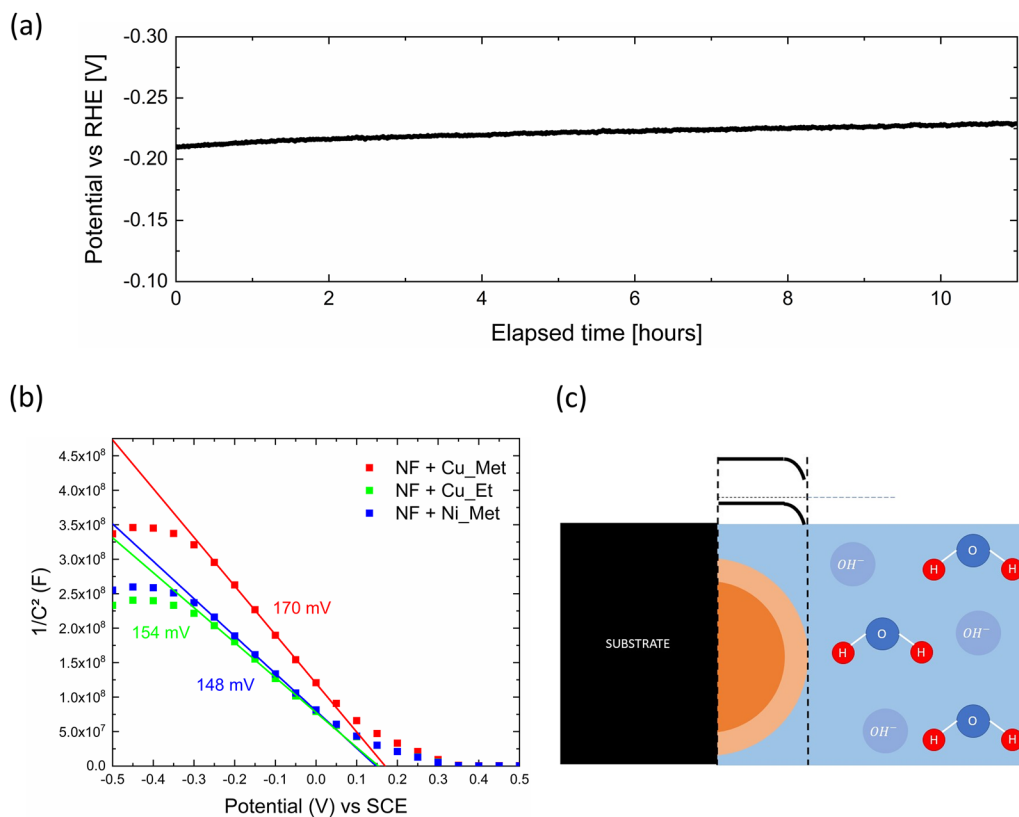


FIG. 6. (a) Chronopotentiometry measurement at $10 \text{ mA}/\text{cm}^2$ for the *Cu_met* electrode for 13 h. (b) Mott-Schottky plot with marked x-intercept of the linear fit. (c) Scheme displaying the catalyst-electrolyte interface and the energy bending below the electrode surface.

TABLE IV. Summary of the electrochemical parameters. η is the overpotential vs RHE at 10 mA/cm²; TS is the Tafel slope; V_{fb} , V_{oc} , and V_{bb} are, respectively, the flat-band potential, the open circuit potential, and the band bending vs SCE.

Electrode	HER		OER		Catalyst loading ($\frac{\mu\text{g}}{\text{cm}^2}$)	Mass activity ($\frac{\text{A}}{\text{mg}}$)	V_{fb} (mV)	V_{oc} (mV)	V_{bb} (mV)
	η (mV)	TS ($\frac{\text{mV}}{\text{dec}}$)	η (mV)	TS ($\frac{\text{mV}}{\text{dec}}$)					
<i>Cu_met</i>	211	90	338	51	0.8	12.5	170	-352	497
<i>Cu_et</i>	224	95	331	51	1.8	9.1	154	-320	481
<i>Ni_met</i>	230	90	327	44	0.7	14.3	148	-340	463

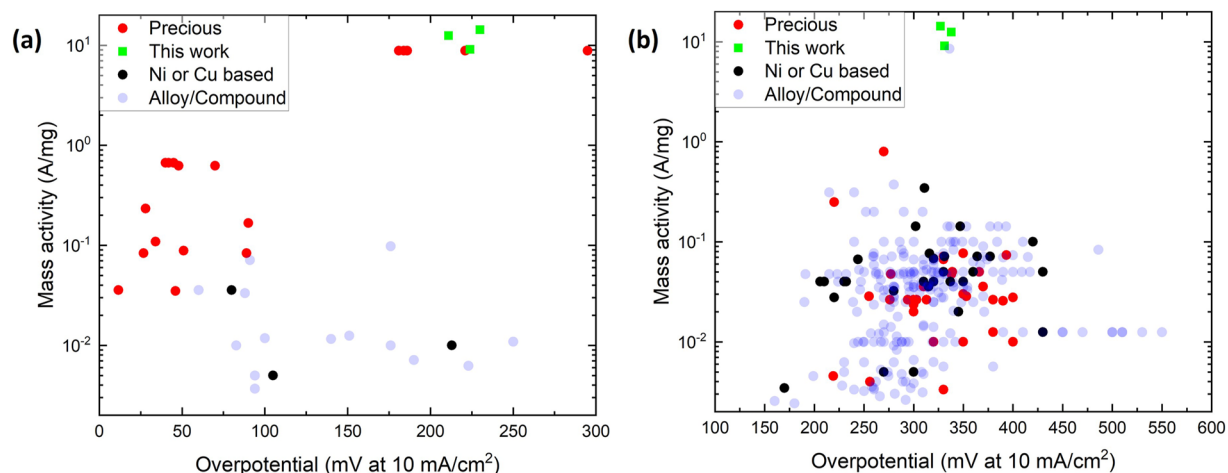


FIG. 7. Literature data from Ref. 2 for (a) HER and (b) OER reporting precious, Ni- and Cu-based, and alloy/compound catalysts with added data from this work.²

First, the open circuit (OC) potential was measured. All the OC measurements resulted in negative values, and the derived flat band potential from MS resulted in positive values [Fig. 6(a)]. Using Eq. (5), all the band bending results in positive values (Table IV), indicating that there is a positive charge accumulation on the electrode-liquid interface [Fig. 6(b) and 6(c)]. A relation occurs between the overpotential and the band bending. In fact, in Table IV, the OER overpotential and band bending are both sorted in the descending order, while the HER overpotential is sorted in the ascending order. Whenever the negative charge accumulated below the surface of the catalyst is higher, the

band bending is thus higher and there are more electrons available for the HER, justifying the lower overpotential obtained for the *Cu_met* electrode.

Figure 7 shows the literature data of the state of the art for both HER and OER in terms of mass activity (in log scale) and overpotential, and the data that lie in the top left region of the graphs are the best. The results found in this work are positioned in the top part of the graph due to the very low amount of catalysts used for both HER and OER characterizations. In Fig. 7(a), the HER data are represented. The red dots represent the performance of platinum catalysts, and the data obtained in this work lie between

TABLE V. Summary of Cu-based and Ni-based electrocatalysts reported in the literature tested for both OER and HER.

Catalyst	Electrolyte and study type	Overpotential (10 mA/cm ²) (mV)	Reference
Nanotubes of CuO	KOH (1M) OER study	320	45
NiFe/Cu(OH) ₂	KOH (1M) OER study	283	46
NF/Cu ₃ P	KOH (1M) OER study	320	47
CuO/Co ₃ O ₄	KOH (1M) HER study	288	48
Poly-polished Cu	KOH (1M) HER study	320	49
CF/rGO/CuO-Cu ₂ O/Cu	KOH (1M) HER study	105	50

these ones. Although the overpotential values obtained with the Cu NPs and Ni NPs are not outstanding, they still represent a valid and inexpensive alternative to precious and rare materials, especially in terms of mass activity. The overpotential can be far improved for these PLAL Cu-based electrodes by increasing the amount of material due to the extrinsic nature of this parameter. Figure 7(b) shows the comparison of different electrodes for alkaline OER. The data obtained in this work are positioned in the top part of the graph, still indicating a high intrinsic activity of our catalysts and a more competitive result in terms of overpotential compared to the literature. The lower values of overpotential for OER are typically obtained with alloys or composite materials and using a higher catalyst loading. Some examples of Ni and Cu-based electrocatalyst tested for OER and HER in 1 M KOH electrolyte are reported in Table V still reflecting how alloying and co-catalyst introduction can be improve the electrochemical performances.

IV. CONCLUSIONS

In this work, copper and nickel NPs were synthesized using PLAL in methanol and ethanol. For both copper and nickel, the solvents chosen prevented the oxidation and, thus, metallic and crystalline NPs with a nanometric mean radius were obtained. From the TEM images, some agglomerates were observed and a carbon/oxygen matrix surrounding the NPs was found mainly for *Cu_{met}* and *Cu_{et}* dispersions. The presence of carbon and oxygen was highlighted by the STEM-EDX measurements and also by the XPS analysis. The crystalline nature of Cu-based NPs was confirmed by the HR-TEM and XRD measurements. The latter demonstrated the metallic nature of *Cu_{met}*, *Ni_{met}*, and also *Cu_{et}* although some oxidation was observed. The NPs produced were loaded ($\sim 1 \mu\text{gcm}^{-2}$) onto a NF substrate and tested for HER and OER in aqueous 1M KOH. The best results, in terms of overpotential, for the HER were observed using the *Cu_{met}* based electrode (211 mV), while for the OER, the lowest overpotential was 327 mV by *Ni_{met}*. By the Mott-Schottky measurements, *Cu_{met}* was found to have the highest band bending, responsible for higher electron accumulation at the interface and, thus, the lowest energy for the HER activation. Afterward, a literature comparison showed that the data found in this work have a high mass activity compared to other non-critical material-based catalysts. The extrinsic catalytic activity represented by the overpotential can still be enhanced with a catalyst loading but represents a competitive result considering the cost-effective and green technique used for the NP production and the lack of critical materials.

SUPPLEMENTARY MATERIAL

The Supplementary material contains additional details regarding the electrode preparation and has more morphological, compositional, and structural analysis results of Cu NPs and Ni NPs obtained in this work.

ACKNOWLEDGMENTS

This work was supported by the project “Programma di ricerca di ateneo UNICT 2020–22 linea 2” of the University of Catania, Italy.

This work was partially funded by European Union (NextGenerationEU), through the MUR-PNRR project SAMOTHRACE (Grant No. ECS0000022). The authors acknowledge the Bio-nanotech Research and Innovation Tower (BRIT) laboratory of the University of Catania (Grant No. PONA3–00136 financed by the MIUR) for the SmartLab diffractometer facility and thank Professor G. Malandrino (uniCT) for kind availability related to XRD measurements and S. Tati, C. Percolla, and G. Pantè (CNR-IMM, Catania University, Italy) for the technical support.

AUTHOR DECLARATIONS

Conflict of Interest

The authors have no conflicts to disclose.

Author Contributions

V. Iacono: Data curation (equal); Formal analysis (equal); Investigation (equal); Methodology (equal); Validation (equal); Writing – original draft (equal); Writing – review & editing (equal). **C. Lo Pò:** Data curation (equal); Formal analysis (equal); Investigation (equal); Methodology (equal); Validation (equal); Writing – original draft (equal); Writing – review & editing (equal). **S. Scalse:** Methodology (equal); Resources (equal); Validation (equal); Writing – review & editing (equal). **S. Boninelli:** Data curation (equal); Formal analysis (equal); Investigation (equal); Methodology (equal); Validation (equal); Writing – review & editing (equal). **G. G. Condorelli:** Investigation (equal); Methodology (equal); Validation (equal); Writing – review & editing (equal). **M. G. Grimaldi:** Funding acquisition (equal); Investigation (equal); Methodology (equal); Supervision (equal); Validation (equal); Writing – review & editing (equal). **F. Ruffino:** Conceptualization (equal); Funding acquisition (equal); Investigation (equal); Methodology (equal); Resources (equal); Supervision (equal); Validation (equal); Writing – review & editing (equal).

DATA AVAILABILITY

The data that support the findings of this study are available within the article and its supplementary material.

REFERENCES

- 1 I. Dincer and C. Acar, “Review and evaluation of hydrogen production methods for better sustainability,” *Int. J. Hydrogen Energy* **40**, 11094–11111 (2015).
- 2 J. Kibsgaard and I. Chorkendorff, “Considerations for the scaling-up of water splitting catalysts,” *Nat. Energy* **4**, 430–433 (2019).
- 3 N.-T. Suen, S.-F. Hung, Q. Quan, N. Zhang, Y.-J. Xu, and H. M. Chen, “Electrocatalysis for the oxygen evolution reaction: Recent development and future perspectives,” *Chem. Soc. Rev.* **46**, 337–365 (2017).
- 4 Deeksha, P. Kour, I. Ahmed, Sunny, S. K. Sharma, K. Yadav, and Y. K. Mishra, “Transition metal-based perovskite oxides: Emerging electrocatalysts for oxygen evolution reaction,” *ChemCatChem* **15**, e202300040 (2023).
- 5 Bhawna, S. Kumar, R. Sharma, S. J. Borah, A. Gupta, M. K. Gupta, R. Kumar, K. K. Dubey, Y. K. Mishra, and V. Kumar, “Catalytic heterostructured materials for CO₂ mitigation and conversion into fuels: A renewable energy approach towards a sustainable environment,” *Sustainable Energy Fuels* **7**, 4354 (2023).

- ⁶S. Trasatti, "Work function, electronegativity, and electrochemical behaviour of metals," *J. Electroanal. Chem. Interfacial Electrochem.* **39**, 163–184 (1972).
- ⁷T. B. Ferriday, P. H. Middleton, and M. L. Kolhe, "Review of the hydrogen evolution reaction—A basic approach," *Energies* **14**, 8535 (2021).
- ⁸M. Gong, D.-Y. Wang, C.-C. Chen, B.-J. Hwang, and H. Dai, "A mini review on nickel-based electrocatalysts for alkaline hydrogen evolution reaction," *Nano Res.* **9**, 28–46 (2015).
- ⁹Z. Zhou, X. Li, Q. Li, Y. Zhao, and H. Pang, "Copper-based materials as highly active electrocatalysts for the oxygen evolution reaction," *Mater. Today Chem.* **11**, 169–196 (2019).
- ¹⁰I. Roger, M. A. Shipman, and M. D. Symes, "Earth-abundant catalysts for electrochemical and photoelectrochemical water splitting," *Nat. Rev. Chem.* **1**, 0003 (2017).
- ¹¹S. Barcikowski, V. Amendola, G. Marzun, C. Rehbock, S. Reichenberger, D. Zhang, and B. Gökce, *Handbook of Laser Synthesis of Colloids* (Duisburg-Essen Publications Online, 2016).
- ¹²E. Fazio, B. Gökce, A. De Giacomo, M. Meneghetti, G. Compagnini, M. Tommasini, F. Waag, A. Lucotti, C. G. Zanchi, P. M. Ossi, M. Dell'Aglio, L. D'Urso, M. Condorelli, V. Scardaci, F. Biscaglia, L. Litti, M. Gobbo, G. Gallo, M. Santoro, S. Trusso, and F. Neri, "Nanoparticles engineering by pulsed laser ablation in liquids: Concepts and applications," *Nanomaterials* **10**, 2317 (2020).
- ¹³N. Lasemi, U. Pacher, C. Rentenberger, O. Bomati-Miguel, and W. Kautek, "Laser-assisted synthesis of colloidal Ni/NiO_x core/shell nanoparticles in water and alcoholic solvents," *ChemPhysChem* **18**, 1118–1124 (2017).
- ¹⁴V. Amendola, D. Amans, Y. Ishikawa, N. Koshizaki, S. Scirè, G. Compagnini, S. Reichenberger, and S. Barcikowski, "Room-temperature laser synthesis in liquid of oxide, metal-oxide core-shells, and doped oxide nanoparticles," *Chem. Eur. J.* **26**, 9206–9242 (2020).
- ¹⁵T. Begildayeva, S. J. Lee, Y. Yu, J. Park, T. H. Kim, J. Theerthagiri, A. Ahn, H. J. Jung, and M. Y. Choi, "Production of copper nanoparticles exhibiting various morphologies via pulsed laser ablation in different solvents and their catalytic activity for reduction of toxic nitroaromatic compounds," *J. Hazard. Mater.* **409**, 124412 (2021).
- ¹⁶T. Begildayeva, D. Chinnadurai, S. J. Lee, Y. Yu, J. K. Song, and M. Y. Choi, "Implementation of novel pulsed laser ablation strategy to control the morphological growth and enrich the electrochemically active sites of multifunctional Ni–CuO electrocatalyst," *J. Alloys Compd.* **901**, 163446 (2022).
- ¹⁷H. J. Jung and M. Y. Choi, "Specific solvent produces specific phase Ni nanoparticles: A pulsed laser ablation in solvents," *J. Phys. Chem. C* **118**, 14647–14654 (2014).
- ¹⁸See <http://www.genplot.com/> for Rump-genplot.
- ¹⁹L. Bruno, S. Battiato, M. Scuderi, F. Priolo, A. Terrasi, and S. Mirabella, "Physical insights into alkaline overall water splitting with NiO microflowers electrodes with ultra-low amount of Pt catalyst," *Int. J. Hydrogen Energy* **47**, 33988–33998 (2022).
- ²⁰S. Anantharaj and S. Noda, "Appropriate use of electrochemical impedance spectroscopy in water splitting electrocatalysis," *ChemElectroChem* **7**, 2297–2308 (2020).
- ²¹N. Krstajić, M. Popović, B. Grgur, M. Vojnović, and D. Šepa, "On the kinetics of the hydrogen evolution reaction on nickel in alkaline solution: Part I. The mechanism," *J. Electroanal. Chem.* **512**(1–2), 16–26 (2001).
- ²²S. Wang, J. Zhang, O. Gharbi, V. Vivier, M. Gao, and M. E. Orazem, "Electrochemical impedance spectroscopy," *Nat. Rev. Methods Primers* **1**, 41 (2021).
- ²³See <http://www.abc.chemistry.bsu.by/vi/analyser/> for Eis spectrum analyzer.
- ²⁴K. Gelderman, L. Lee, and S. W. Donne, "Flat-band potential of a semiconductor: Using the Mott–Schottky equation," *J. Chem. Educ.* **84**, 685 (2007).
- ²⁵K. Sivula, "Mott–Schottky analysis of photoelectrodes: Sanity checks are needed," *ACS Energy Lett.* **6**, 2549–2551 (2021).
- ²⁶M. Quinten, *Optical Properties of Nanoparticle Systems* (Wiley-VCH Verlag, Weinheim, Germany, 2011).
- ²⁷K.-H. Chang, *Reliability analysis, E-Design* (Elsevier, 2015), pp. 523–595.
- ²⁸C. G. Granqvist and R. A. Buhrman, "Log-normal size distributions of ultrafine metal particles," *Solid State Commun.* **18**, 123–126 (1976).
- ²⁹See <https://www.gatan.com/products/tem-analysis/gatan-microscopy-suite-software> for Gatan microscopy suit software.
- ³⁰See <http://carine.crystallography.pagesperso-orange.fr/> for Carine crystallography.
- ³¹M. Klinger, *CrysTBox—Crystallographic Toolbox* (Institute of Physics of the Czech Academy of Sciences, Prague, 2015).
- ³²Pdf Card No.: 00-004-0836 quality:s.
- ³³Pdf Card No.: 00-089-5895 quality:c.
- ³⁴Pdf Card No.: 00-077-0199 quality:c.
- ³⁵Pdf Card No.: 00-004-0850 quality:s.
- ³⁶Pdf Card No.: 00-047-1049 quality:s.
- ³⁷D. Zhang, C. Zhang, J. Liu, Q. Chen, X. Zhu, and C. Liang, "Carbon-encapsulated metal/metal carbide/metal oxide core-shell nanostructures generated by laser ablation of metals in organic solvents," *ACS Appl. Nano Mater.* **2**, 28–39 (2018).
- ³⁸J. F. Moulder, W. F. Stickle, and P. E. Sobol, *Handbook of X-Ray Photoelectron Spectroscopy* (Perkin-Elmer, Physical Electronics Division, 1992).
- ³⁹A. N. Oraevskii, V. P. Pimenov, A. A. Stepanov, and V. A. Shcheglov, "Laser polymerization in gases," *Sov. J. Quantum Electron.* **4**, 711–712 (1974).
- ⁴⁰I. N. Kal'vina, V. F. Moskalenko, E. P. Ostapchenko, L. L. Pavlovskii, T. V. Protzenko, and V. I. Rychkov, "Resonant action of laser radiation on polymerization processes," *Sov. J. Quantum Electron.* **4**, 1285–1286 (1975).
- ⁴¹B. R. Coad, T. Scholz, K. Vasilev, J. D. Hayball, R. D. Short, and H. J. Griesser, "Functionality of proteins bound to plasma polymer surfaces," *ACS Appl. Mater. Interfaces* **4**, 2455 (2012).
- ⁴²H. D. Hazrati, J. D. Whittle, and K. Vasilev, "A mechanistic study of the plasma polymerization of ethanol," *Plasma Processes Polym.* **11**, 149–157 (2014).
- ⁴³P. Marabotti, S. Peggiani, A. Vidale, and C. Spartaco Casari, "Pulsed laser ablation in liquid of sp-carbon chains: Status and recent advances," *Chin. Phys. B* **31**, 125202 (2022).
- ⁴⁴S. Filice, R. Fiorenza, R. Reitano, S. Scialese, S. Scirè, G. Fiscaro, I. Deretzis, A. La Magna, C. Bongiorno, and G. Compagnini, "TiO₂ colloids laser-treated in ethanol for photocatalytic H₂ production," *ACS Appl. Nano Mater.* **3**, 9127–9140 (2020).
- ⁴⁵F. Arshad, A. Munir, Q. Q. Kashif, T. Haq, J. Iqbal, F. Sher, and I. Hussain, "Controlled development of higher-dimensional nanostructured copper oxide thin films as binder free electrocatalysts for oxygen evolution reaction," *Int. J. Hydrogen Energy* **45**, 16583–16590 (2020).
- ⁴⁶X. Ma, X. Li, A. D. Jagadale, X. Hao, A. Abudula, and G. Guan, "Fabrication of Cu(OH)₂@NiFe-layered double hydroxide catalyst array for electrochemical water splitting," *Int. J. Hydrogen Energy* **41**, 14553–14561 (2016).
- ⁴⁷A. Han, H. Zhang, R. Yuan, H. Ji, and P. Du, "Crystalline copper phosphide nanosheets as an efficient Janus catalyst for overall water splitting," *ACS Appl. Mater. Interfaces* **9**, 2240–2248 (2017).
- ⁴⁸A. Tahira, Z. H. Ibupoto, M. Willander, and O. Nur, "Advanced Co₃O₄-CuO nano-composite based electrocatalyst for efficient hydrogen evolution reaction in alkaline media," *Int. J. Hydrogen Energy* **44**, 26148–26157 (2019).
- ⁴⁹P. Farinazzo Bergamo Dias Martins, P. Papa Lopes, E. A. Ticianelli, V. R. Stamenkovic, N. M. Markovic, and D. Strmcnik, "Hydrogen evolution reaction on copper: Promoting water dissociation by tuning the surface oxophilicity," *Electrochem. Commun.* **100**, 30–33 (2019).
- ⁵⁰L. Ye and Z. Wen, "Self-supported three-dimensional Cu/Cu₂O-CuO/rGO nanowire array electrodes for an efficient hydrogen evolution reaction," *Chem. Commun.* **54**, 6388–6391 (2018).